Monthly Notices
of the
ROYAL ASTRONOMICAL SOCIETY

MNRAS **449,** 809–819 (2015) doi:10.1093/mnras/stv287

Characterizing extragalactic anomalous microwave emission in NGC 6946 with CARMA

Brandon Hensley,[1]★ Eric Murphy[2] and Johannes Staguhn[3,4]

[1]*Department of Astrophysical Sciences, Princeton University, Princeton, NJ 08544, USA*
[2]*Spitzer Science Center, California Institute of Technology, 1200 East California Boulevard, Pasadena, CA 91125, USA*
[3]*The Henry A. Rowland Department of Physics and Astronomy, Johns Hopkins University, 3400 North Charles Street, Baltimore, MD 21218, USA*
[4]*Observational Cosmology Lab, Code 665, NASA Goddard Space Flight Center, Greenbelt, MD 20771, USA*

Accepted 2015 February 9. Received 2015 January 19; in original form 2014 November 25

ABSTRACT

Using 1 cm and 3 mm observations from the Combined Array for Research in Millimeter-wave Astronomy and 2 mm observations from the Goddard IRAM Superconducting 2 Millimeter Observer observations, we follow up the first extragalactic detection of anomalous microwave emission (AME) reported by Murphy et al. in an extranuclear region (Enuc. 4) of the nearby face-on spiral galaxy NGC 6946. We find the spectral shape and peak frequency of AME in this region to be consistent with models of spinning dust emission. However, the strength of the emission far exceeds the Galactic AME emissivity given the abundance of polycyclic aromatic hydrocarbons (PAHs) in that region. Using our galaxy-wide 1 cm map (21 arcsec resolution), we identify a total of eight 21 arcsec × 21 arcsec regions in NGC 6946 that harbour AME at >95 per cent significance at levels comparable to that observed in Enuc. 4. The remainder of the galaxy has 1 cm emission consistent with or below the observed Galactic AME emissivity per PAH surface density. We probe relationships between the detected AME and dust surface density, PAH emission, and radiation field, though no environmental property emerges to delineate regions with strong versus weak or non-existent AME. On the basis of these data and other AME observations in the literature, we determine that the AME emissivity per unit dust mass is highly variable. We argue that the spinning dust hypothesis, which predicts the AME power to be approximately proportional to the PAH mass, is therefore incomplete.

Key words: radiation mechanisms: general – ISM: general – radio continuum: ISM.

1 INTRODUCTION

Anomalous microwave emission (AME) is dust-correlated emission observed between ∼20–50 GHz that cannot be accounted for by extrapolating the thermal dust emission to low frequencies. First detected as an emission excess in the microwave (Kogut et al. 1996; de Oliveira-Costa et al. 1997; Leitch et al. 1997), AME is now thought to arise from electric dipole emission from very small grains with size ∼3.5–10 Å that spin rapidly due to the action of systematic torques in the interstellar medium (Draine & Lazarian 1998b; Hoang, Draine & Lazarian 2010; Ysard & Verstraete 2010; Silsbee, Ali-Haïmoud & Hirata 2011). Subsequent Galactic observations have been well-fitted with the inclusion of a spinning dust component (e.g. Miville-Deschênes et al. 2008; Planck Collaboration XX 2011b).

Murphy et al. (2010) reported the first extragalactic detection of AME in a star-forming extranuclear region of the spiral galaxy NGC 6946 (hereafter Enuc. 4). NGC 6946, located at a distance of 6.8 Mpc (Karachentsev, Sharina & Huchtmeier 2000), is known for its intense star formation, having hosted at least nine supernovae in the last century (Prieto et al. 2008) and having a star formation rate (SFR) of 7.1 $M_\odot$ yr^{-1} (Kennicutt et al. 2011). Follow-up observations of Enuc. 4 by the Arcminute Microkelvin Imager (AMI) support the presence of an AME component in this source (Scaife et al. 2010).

To date, additional extragalactic detections have proven elusive. *Planck* observations of the Small Magellanic Cloud (SMC) have shown evidence for an AME component (Planck Collaboration XVII 2011a; Draine & Hensley 2012), but the interpretation is complicated by additional excess emission possibly arising from the large grains. Despite microwave observations of other dusty, star-forming galaxies including Andromeda, only upper limits on an AME component have been placed (Peel et al. 2011; Ade et al. 2014). The difficulty in finding extragalactic AME has hindered our

★ E-mail: bhensley@princeton.edu

ability to probe variations of AME properties within a galaxy, particularly identifying the hallmarks of regions with strong emission.

In this work, we use high-resolution data from the Combined Array for Research in Millimeter-wave Astronomy (CARMA) at 1 cm and 3 mm to better constrain the spectral energy distribution (SED) of Enuc. 4. We combine these CARMA observations with data from *Spitzer*, *Herschel*, the Goddard IRAM Superconducting 2 Millimeter Observer (GISMO), the Very Large Array (VLA), and the Westerbork Synthesis Radio Telescope (WSRT) to create composite SEDs that allow us to decompose the emission into components from thermal dust, synchrotron, free–free, and AME. We compare the AME found in Enuc. 4 to that observed in the Galaxy and assess the viability of the spinning dust mechanism for explaining the emission.

The CARMA 1 cm map provides coverage of the whole galaxy, enabling a search for AME beyond Enuc. 4. As we find multiple additional regions with AME, we use the high-resolution dust model fitting of NGC 6946 by Aniano et al. (2012) to explore correlations between the AME and local properties such as dust surface density, polycyclic aromatic hydrocarbon (PAH) emission, and the intensity of the local radiation field.

We have organized the paper as follows: in Section 2, we describe the data used in this analysis and our data reduction; in Section 3, we perform fits to the SEDs using models for emission from thermal dust, free–free, synchrotron, and AME and analyse the results of the fits for particular regions of the Galaxy; in Section 4, we analyse galaxy-wide correlations between AME and local galaxy properties and comment on the nature of the AME observed in NGC 6946 versus Galactic observations; in Section 5, we discuss the implications of our observations for spinning dust theory; and in Section 6, we summarize our conclusions.

2 DATA REDUCTION AND SED SYNTHESIS

In this section, we describe the data sets used in our analysis. The properties of all maps are summarized in Table 1. The CARMA and GISMO maps were broadened to a common 21 arcsec resolution by convolution with a Gaussian beam while the remaining data were convolved as described in Aniano et al. (2011). 21 arcsec corresponds to a physical scale of about 700 pc at the distance of NGC 6946.

2.1 CARMA data

CARMA consists of 23 antennas – six 10 m, nine 6 m, and eight 3.5 m. The CARMA 3 mm data were taken with 6 and 10 m antennas in the CARMA E configuration with baseline lengths between 8.5 and 66 m in 2010 July. The map has a resolution of 9.1 arcsec and an rms noise level of 0.017 MJy sr^{-1}. The CARMA 1 cm data were taken with the eight 3.5 m Sunyaev-Zel'dovich Array antennas in 2010 October and 2011 July using both the SH and SL configurations. The map has a resolution of 18.8 arcsec and an rms noise level of 0.016 MJy sr^{-1}. The data were reduced with MIRIAD (Sault, Teuben & Wright 2011) using Mars, Jupiter, and Uranus as flux calibrators and assuming a 10 per cent calibration uncertainty. A primary beam correction was applied to both maps. We present the emission contours from these maps in Fig. 1.

2.2 GISMO Data

GISMO is a Transition Edge Sensor bolometer camera on the IRAM 30 m telescope that operates in the 2 mm atmospheric window (Staguhn et al. 2008, 2014). A total of 1.5 h of integration time was obtained on Enuc 4 in 2013 April at 17 arcsec resolution. The data were reduced using the CRUSH software package 'deep mode' (Kovács 2008), which includes large-scale filtering to mitigate atmospheric effects.

2.3 Ancillary data

2.3.1 IR data

NGC 6946 was part of both the *Spitzer* Infrared Nearby Galaxies Survey (SINGS; Kennicutt et al. 2003) and Key Insights on Nearby Galaxies: a Far-Infrared Survey with *Herschel* (KINGFISH; Kennicutt et al. 2011) projects, and thus has extensive *Spitzer* and *Herschel* observations. We use the same data set detailed in Aniano et al. (2012) consisting of 3.6, 4.5, 5.8, and 8.0 μm IRAC images and 24 and 70 μm MIPS images from SINGS, and 70, 100, and 160 μm

Table 1. Data summary.

Instrument	λ (μm)	FWHM (arcsec)	$\sigma_{\rm rms}$ (MJy sr^{-1})	$\sigma_{\rm Calibration}$ (per cent)	Reference
IRAC	3.6	1.90	0.0093	5	Aniano et al. (2012)
IRAC	4.5	1.81	0.0093	5	Aniano et al. (2012)
IRAC	5.8	2.11	0.0274	5	Aniano et al. (2012)
IRAC	8.0	2.82	0.0356	5	Aniano et al. (2012)
MIPS	24	6.43	0.0328	5	Aniano et al. (2012)
MIPS	70	18.7	0.334	10	Aniano et al. (2012)
PACS	70	5.67	2.52	10	Aniano et al. (2012)
PACS	100	7.04	2.22	10	Aniano et al. (2012)
PACS	160	11.2	1.53	20	Aniano et al. (2012)
SPIRE	250	18.2	0.873	15	Aniano et al. (2012)
GISMO	2000	17.0	0.060	10	This work
CARMA	3000	9.1	0.017	10	This work
CARMA	10 000	18.8	0.016	10	This work
VLA	30 000	14	0.010	5	Braun et al. (2007)
VLA	60 000	14	0.011	5	Braun et al. (2007)
VLA	18 000	14	0.006	5	Braun et al. (2007)
VLA	20 000	14	0.006	5	Braun et al. (2007)
WSRT	22 000	15	0.004	5	Beck (2007)

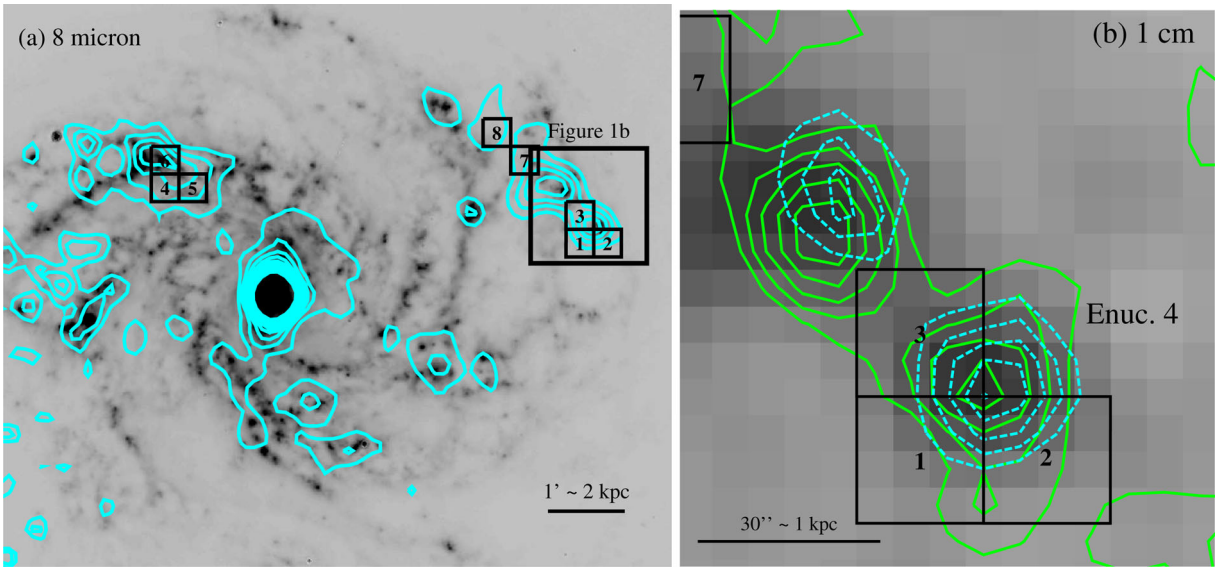

Figure 1. Left: we overlay the emission contours from the 1 cm map on the IRAC 8 μm image, where the 10 contour levels are linearly spaced between the 3σ noise level of 0.048 MJy sr^{-1} and 0.48 MJy sr^{-1}. The eight pixels with significant AME detections are shown in black boxes with numbering corresponding to Table 2. Right: we overlay the emission contours from the 2 mm (green solid) and 3 mm (cyan dashed) maps on the 1 cm image in the Enuc. 4 region (indicated by the solid rectangle in the left-hand panel), demonstrating excellent coincidence of the emission in all three maps. The five 2 mm contours are linearly spaced between 0.05 and 0.2 MJy sr^{-1} while the five 3 mm contours are linearly spaced between 0.04 and 0.13 MJy sr^{-1}.

PACS images and a 250 μm SPIRE image from KINGFISH. We do not use the 160 μm MIPS image or the SPIRE 350 or 500 μm images due to insufficient angular resolution. All of the remaining images have resolution better than our 18.8 arcsec CARMA 1 cm map.

2.3.2 *Radio data*

We employ the same radio data as Murphy et al. (2010). These consist of the 1.4 GHz radio map from the WSRT-SINGS survey (Braun et al. 2007) with a 14 arcsec × 12.5 arcsec beam and VLA maps at 1.5, 1.7, 4.9, and 8.5 GHz, all with 15 arcsec × 15 arcsec beams (Beck 2007).

3 ENUC. 4

The new observations at 1 cm and 3 and 2 mm allow us to revisit the SED of Enuc. 4 obtained by Murphy et al. (2010) and place tighter constraints on the frequency-dependence of the AME. In particular, the inclusion of the 2 and 3 mm data allow us to better constrain the sum of the AME and thermal dust contributions and verify the presence of a spectral peak in the 30 GHz range. We extract the flux density in a 21 arcsec diameter circular aperture centred on the Enuc. 4 position given by Murphy et al. (2010).

3.1 Fits without spinning dust

We first attempt to fit the Eunc. 4 SED without invoking a spinning dust component. We model the synchrotron emission as a power law with unknown normalization and index, i.e.

$$F_\nu^{\rm sync} = A\left(\frac{\nu}{1.36\,{\rm GHz}}\right)^{-\alpha_{\rm sync}}. \quad (1)$$

We adopt two fitting strategies for the synchrotron slope. Guided by the results of Niklas, Klein & Wielebinski (1997), in the first approach we put a Gaussian prior with mean 0.83 and standard deviation 0.13 on $\alpha_{\rm sync}$. This is a safeguard against fits that yield unphysically low values of $\alpha_{\rm sync}$ to compensate enhanced 1 cm emission. In the second, we simply draw values for $\alpha_{\rm sync}$ uniformly between 0.5 and 1.5. Our results are robust to this choice, and thus we adopt the latter as the default for its simplicity. To fit the amplitude, we expect that the synchrotron comprises the majority of the emission at 22 cm and therefore draw the synchrotron normalization A uniformly between 0 and the 5σ upper limit on the 22 cm data point.

It is unclear whether a power law is a good description of the synchrotron emission over the frequency range of interest. In particular, the Galactic synchrotron index has been observed to steepen by ∼0.3 between 13 and 1 cm in analyses of *Wilkinson Microwave Anisotropy Probe* (*WMAP*) and *Planck* data (e.g. Bennett et al. 2003; Planck Collaboration 2014a). Such steepening is expected when electrons with requisite energy are no longer able to be produced. Our data have insufficient frequency sampling to meaningfully constrain a break frequency or the resulting index. Therefore, we consider the extreme case in which the synchrotron produces no emission below 3 cm. Although this will not substantially affect the modelling of the emission in Enuc. 4, steepening is required to explain the SED of other regions of the galaxy, as discussed in detail in Section 4.

We model the free–free emission as a power law with fixed index −0.12 and unknown normalization, i.e.

$$F_\nu^{\rm ff} = B\left(\frac{\nu}{30\,{\rm GHz}}\right)^{-0.12}. \quad (2)$$

Because we possess the full infrared SED of the galaxy, we can constrain the free–free emission based on the empirical relations from Murphy et al. (2012) connecting the thermal emission, 24 μm flux density, and total IR luminosity to the SFR. Combining their equations (6) and (14) and assuming an electron temperature of 10^4 K, we obtain

$$F_{\nu,1\,{\rm cm}}^{\rm ff} = 4.74\times10^{-3}F_{\nu,24\,\mu{\rm m}}. \quad (3)$$

Likewise, combining their equations (6) and (15), we obtain

$$(\nu L_\nu)^{\rm ff}_{1\,\rm cm} = 1.46 \times 10^{-6} L_{\rm IR}. \quad (4)$$

The total IR luminosity from dust has been estimated for each pixel by Aniano et al. (2012, their equations 14 and 21) by fitting the infrared SED with the Draine & Li (2007) dust model, and we use this value as $L_{\rm IR}$ here.

We adopt two approaches to fit the free–free. In the first, we draw B uniformly between half the minimum and twice the maximum values computed with equations (3) and (4), which should accommodate both variations in electron temperature and intrinsic scatter in the relations (Murphy et al. 2011, 2012). In the second, we draw uniformly between 0 and the 5σ upper limit on the 1 cm emission. We find that our results are robust to choice of prior and adopt the latter method as the default for its simplicity.

For the thermal dust component, we assume a power law of the form

$$F_\nu = C \left(\frac{\nu}{150\,\rm GHz}\right)^\beta, \quad (5)$$

where we fix $\beta = 3.65$ in accord with measurements of the thermal dust SED by *Planck* and draw C uniformly between 0 and the 5σ upper limit on the 2 mm (150 GHz) data point.

To perform the fit, we make 2×10^5 draws from the prescribed distribution for each of the j model parameters p_j, then explicitly compute the likelihood $\mathcal{L}_k$ of the model defined by the parameters p_j for each draw k,

$$\mathcal{L}_k \propto \prod_i {\rm e}^{-\frac{(\hat{F}_i - F_i)^2}{2\sigma_i^2}}, \quad (6)$$

where the $\hat{F}_i$ is the flux density estimated by the model at frequency i given the p_j and F_i is the data at frequency i that has error σ_i. The proportionality constant has been omitted since we compare only the relative likelihood of models. We then construct the estimator

$$\hat{p}_j = \frac{\sum_k \mathcal{L}_k p_j}{\sum_k \mathcal{L}_k} \quad (7)$$

for each p_j. Finally, we find the 1D confidence intervals for each parameter p_j by noting the value of p_j such that the sum of the likelihoods of all models with more extreme values of p_j is the appropriate fraction of the sum of the likelihoods of all trials. We obtain nearly identical results on repeating this process, indicating that the number of draws is sufficiently high to sample to the parameter space.

Fig. 2(a) gives the fit of these three components to the data, which is poor.

3.2 Spinning dust fits

We perform a second fit employing an additional component from spinning dust emission. Spinning dust emission is a complicated process that depends upon the size, shape, and charge of the emitting grains as well as the environmental conditions such as gas temperature, molecular fraction, ionization state, and the intensity of the radiation field. Fitting a model that varies all of these parameters is well beyond the capabilities of the data, thus we seek instead a simple prescription for the emission. Following Draine & Hensley (2012), we parametrize the spinning dust emission as

$$F_\nu^{\rm sd} = D \left(\frac{\nu}{\nu_0}\right)^2 \exp\left[1 - \left(\frac{\nu}{\nu_0}\right)^2\right], \quad (8)$$

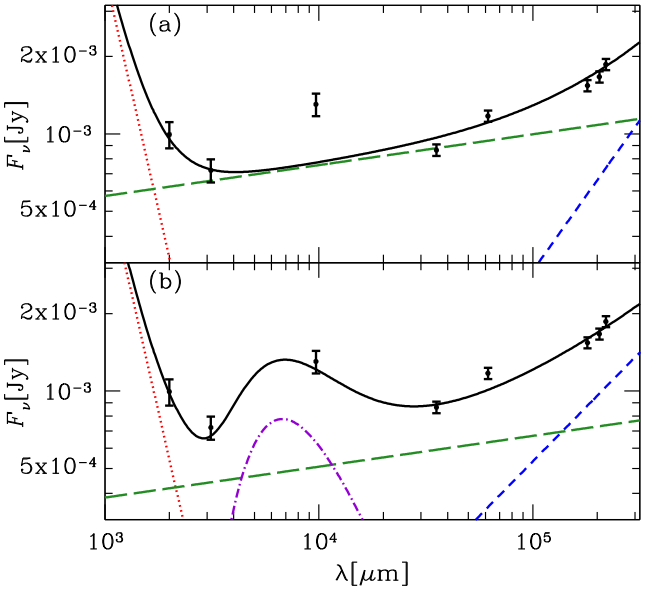

Figure 2. The fit to the long wavelength Enuc. 4 SED using only free–free (long dashed green), synchrotron (short dashed blue), and thermal dust emission (dotted red) is plotted in panel (a) while the fit in panel (b) includes a contribution from spinning dust emission (dot–dashed violet). The total emission for each model is plotted with a solid black line. The goodness of fit is improved considerably with the inclusion of an AME component with peak frequency 44 GHz and amplitude 0.76 mJy at peak.

where the peak frequency ν_0 and the amplitude D are free parameters. We restrict ν_0 to be between 10 and 70 GHz and D to be between 0σ and the 5σ upper limit on the 1 cm data point. Although the model is a simplification of the underlying physics, it is nevertheless instructive to compare both the amplitude and peak frequency obtained from the fits to those of similar studies performed in the Galaxy.

Using the formalism outlined above, we obtain $D = 0.76 \pm 0.23$ mJy and $\nu_0 = 44 \pm 6$ GHz, corresponding to a 30 GHz flux density of 0.61 mJy. The free–free flux density at 1 cm is 5.1×10^{-4} Jy, a factor of 2 above the 2.4×10^{-4} Jy estimate from $F_{\nu,24\,\mu\rm m}$ but less than what was required by the fit with no spinning dust emission. The 5.9×10^{-4} Jy of free–free required by the fit at 3 cm exceeds the estimate of 2.7×10^{-4} Jy by a similar factor.

Fig. 2(b) presents the much improved fit using this model. To quantify the improvement, we perform the likelihood ratio test by constructing the test statistic $\mathcal{D}$,

$$\mathcal{D} = -2 \ln \mathcal{L}_1 + 2 \ln \mathcal{L}_2, \quad (9)$$

where $\mathcal{L}_1$ and $\mathcal{L}_2$ are the likelihoods of the best-fitting models without and with a spinning dust component, respectively. $\mathcal{D}$ follows a χ^2 distribution with the number of degrees of freedom equal to the difference in the number of free parameters in the two models, here two. We obtain $\mathcal{D} = 13.8$, disfavouring the model with no spinning dust emission with $p \simeq 10^{-3}$.

3.3 Thermal dust fits

Having fit the radio data, we now perform a more realistic modelling of the thermal dust emission. We follow the fitting strategy of Aniano et al. (2012) and employ the Draine & Li (2007) dust model. This model includes populations of silicate and carbonaceous grains, including a PAH population, heated by a distribution

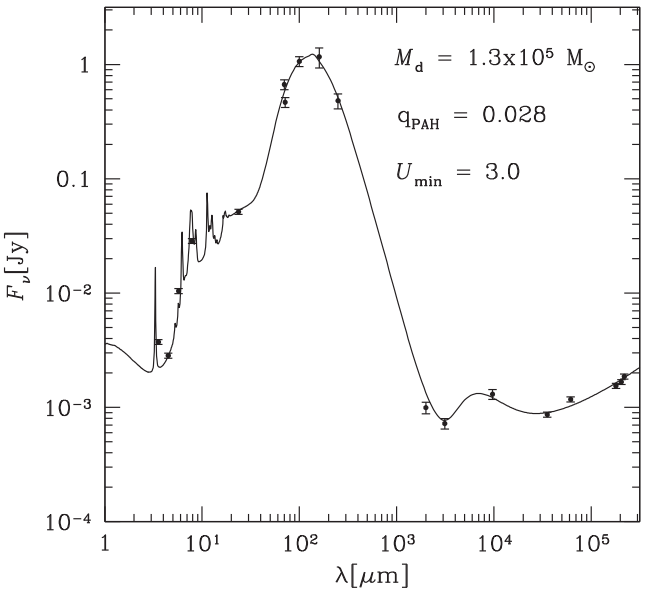

Figure 3. The full SED of Enuc. 4 extracted from a 21 arcsec diameter circular aperture (corresponding to a physical scale of $\simeq$ 700 pc) with the best-fitting model overlaid.

of radiation field intensities such that the differential dust mass $\mathrm{d}M_\mathrm{d}$ heated by starlight intensities between U and $U + \mathrm{d}U$ is given by

$$\frac{1}{M_\mathrm{d}}\frac{\mathrm{d}M_\mathrm{d}}{\mathrm{d}U} = (1-\gamma)\,\delta\,(U-U_\mathrm{min}) + \gamma\,\frac{\alpha-1}{U_\mathrm{min}^{1-\alpha}+U_\mathrm{max}^{1-\alpha}}\,U^{-\alpha} \qquad (10)$$

for $U_\mathrm{min} < U < U_\mathrm{max}$. The heating spectrum is assumed to be the interstellar radiation field determined by Mathis, Mezger & Panagia (1983) scaled by a constant factor U. U_min, U_max, γ, and α, are free parameters of the model to be fit. The PAH emission features require the addition of the parameter q_PAH defined as the total mass fraction of the dust in PAHs. Following Aniano et al. (2012), we set $U_\mathrm{max} = 10^7$ since most pixels in NGC 6946 were best-fitted by this value and the model is in general relatively insensitive to the value of this parameter (Draine et al. 2007). We define $\bar{U}$ as the dust mass-weighted mean starlight intensity heating the dust.

We fit this model to the Enuc. 4 SED 3 mm and shortwards after subtracting the best-fitting synchrotron, free–free, and synchrotron as determined in Section 3.2. The thermal dust fit presented in Fig. 3 has fit parameters $q_\mathrm{PAH} = 0.028$, $M_\mathrm{d} = 1.3 \times 10^5\,\mathrm{M}_\odot$, $U_\mathrm{min} = 3$, $\alpha = 1.7$, and $\gamma = 1.1 \times 10^{-3}$. f_PDR, the fraction of the dust luminosity radiated from regions with $U > 100$, has a value of 0.18.

3.4 Comparisons to spinning dust models

For reasonable assumptions about the size distribution and electric dipole moments of small grains, Draine & Lazarian (1998a,b) calculated a spinning dust emissivity at 30 GHz of 1×10^{-17} Jy sr^{-1} cm^2 H^{-1}, consistent with the observations of Kogut et al. (1996), de Oliveira-Costa et al. (1997), and Leitch et al. (1997), though the scatter was large. Subsequent observations of the Hα-correlated AME (Dobler, Draine & Finkbeiner 2009), the Perseus molecular cloud (Tibbs et al. 2010, 2011), an ensemble of Galactic clouds (Planck Collaboration XV 2014b), and the average diffuse ISM (Planck Collaboration XVII 2014c) have all suggested a lower emissivity of about 3×10^{-18} Jy sr^{-1} cm^2 H^{-1}. We adopt this as our benchmark value.

Since spinning dust emission arises from the smallest grains (believed to be PAHs), its flux density should be directly proportional to the mass of small grains present, i.e. $M_\mathrm{PAH} \equiv q_\mathrm{PAH} M_\mathrm{d}$. It is therefore more appropriate to normalize the AME by PAH mass rather than by hydrogen column. Using the Galactic values of $q_\mathrm{PAH} = 0.046$ and $M_\mathrm{d}/M_\mathrm{H} = 0.01$ (Draine & Li 2007), a spinning dust emissivity of 3×10^{-18} Jy sr^{-1} cm^2 H^{-1}, and taking the distance to NGC 6946 to be 6.8 Mpc (Karachentsev et al. 2000), we obtain

$$F_\nu^\mathrm{sd} = 2 \times 10^{-8}\,\frac{M_\mathrm{PAH}}{\mathrm{M}_\odot}\,\mathrm{Jy}. \qquad (11)$$

From the values of q_PAH and M_d that were derived from fitting the thermal dust emission, equation (11) implies $F_\nu^\mathrm{sd} = 0.06$ mJy of spinning dust emission in Enuc. 4. This is more than a factor of 10 below the fit value of 0.61 mJy and discrepant at 3σ. The emissivity observed in Enuc. 4 corresponds to 2×10^{-7} Jy/M_PAH.

Theoretical models of spinning dust emission predict that the peak frequency is sensitive to the environment, in particular the gas density. The peak frequency derived here agrees well with models of the Cold Neutral Medium (CNM) and Warm Ionized Medium (WIM) presented by Draine & Lazarian (1998a,b), but disfavour the low-frequency ($\simeq$20 GHz) peak predicted by models of spinning emission arising from the Warm Neutral Medium (WNM).

Other large-scale determinations of the AME peak frequency have also yielded results around 40 GHz. The all-sky AME SED extracted from *WMAP* (Miville-Deschênes et al. 2008) was fit in part using a CNM component peaking at $\simeq$40 GHz by Hoang, Lazarian & Draine (2011) and Ysard, Miville-Deschênes & Verstraete (2010). However, both models also required a dominant WNM component peaking at $\simeq$23 GHz that we do not see here. Additionally, Hα-correlated AME was found to peak around 40 GHz (Dobler et al. 2009), consistent with spinning dust in the WIM. Stepping outside the Galaxy, the millimeter SMC SED is well-fitted using a spinning dust contribution peaking at 40 GHz (Draine & Hensley 2012).

We thus conclude that the AME detected in Enuc. 4 has a spectral shape and peak frequency consistent with spinning dust emission from the CNM or WIM as seen in both the Galaxy and the SMC, but is far stronger than Galactic AME per unit PAH mass. It is possible that the dust in NGC 6946 is substantially different than Galactic dust in composition, leading to an increased spinning dust emissivity. To better understand the evolution of AME strength with environment, we investigate other regions in NGC 6946 with detected AME in the following section.

4 GALAXY-WIDE ANALYSIS

Though centred on Enuc. 4, our CARMA 1 cm map provides coverage over the entire galaxy. We can therefore leverage the dust fitting by Aniano et al. (2012) to determine whether correlations exist between the fit AME emissivity and the dust properties of that location. To our knowledge, this is the first time such an analysis has been conducted over such a large scale in an external galaxy.

4.1 Model fitting

We first regridded the maps at each frequency to 21 arcsec $\times$ 21 arcsec square pixels in order to minimize pixel-to-pixel correlations. The 2 and 3 mm maps were not used in this analysis as they cover only the region of the galaxy immediately surrounding Enuc. 4. To ensure that we are fitting galaxy and not background pixels, we require a 3σ detection in all IR and radio bands *except* the 1 cm

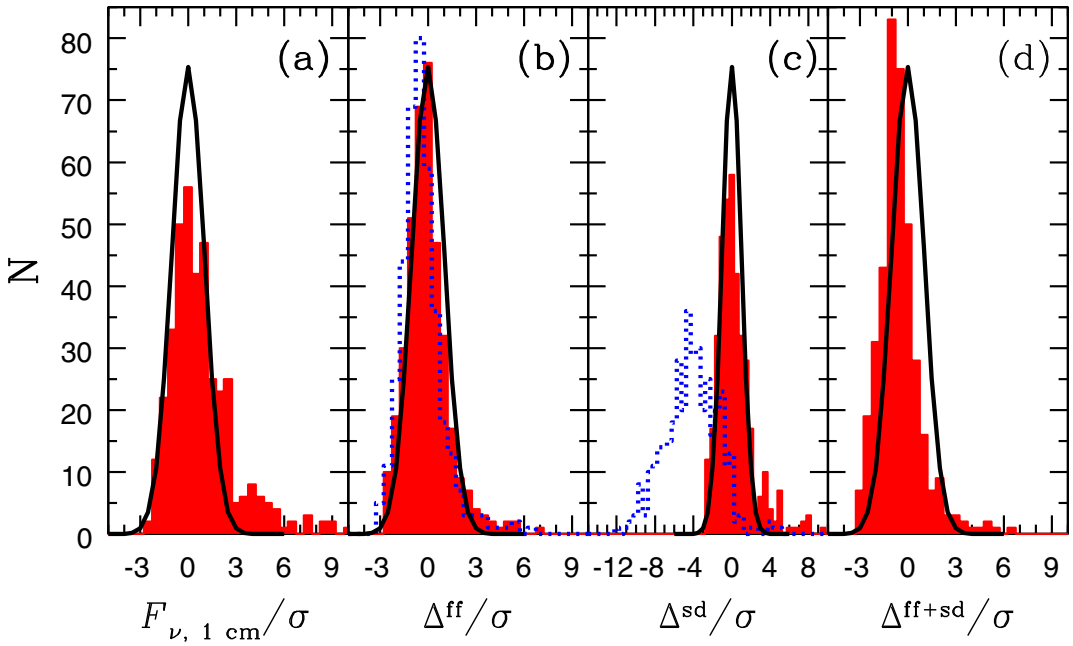

Figure 4. In all panels, we plot a histogram of the expected number of items in each 0.5σ bin assuming 382 points are drawn from a Gaussian distribution of mean 0 and standard deviation σ (black). In panel (a), we plot the histogram of 1 cm flux densities normalized by the observational error (red filled). The noise in the map appears adequately estimated. In panel (b), we subtract estimates of the free–free emission from $F_{\nu,1\,\mathrm{cm}}$ and normalize the difference by the 1 cm error, i.e. $\Delta^{\mathrm{ff}} = F_{\nu,1\,\mathrm{cm}} - F^{\mathrm{ff}}_{\nu 1\,\mathrm{cm}}$. The estimate for free–free emission using $F_{\nu 24\,\mu\mathrm{m}}$ (red filled) appears more consistent with the data than the estimate for free–free emission using L_{IR} (blue dotted). In panel (c), we perform a similar subtraction for estimates of the spinning dust emission from equation (11) (red filled) and the emissivity implied by our fit to Enuc. 4 (blue dotted), i.e. $\Delta^{\mathrm{sd}} = F_{\nu,1\,\mathrm{cm}} - F^{\mathrm{sd}}_{\nu,1\,\mathrm{cm}}$. It is clear that even before accounting for free–free and synchrotron, the emissivity per PAH observed in Enuc. 4 is inconsistent with most regions of the galaxy. Finally in panel (d), we perform a final subtraction using *both* the free–free estimate based on $F_{\nu,24\,\mu\mathrm{m}}$ and equation (11). The fit is generally good, though one or both components may be overestimated. Also, there are clear outliers indicating the entirety of the emission in some pixels has not been accounted for.

band, where it is useful to place upper limits on the AME contribution. We note that using a 5σ threshold does not substantially affect the results, but does reduce the number of pixels considered.

Before performing a fit to the radio SED, we consider the 1 cm map alone. In Fig. 4(a), we present the histogram of 1 cm flux densities normalized by the 1σ error for the 382 pixels meeting the 3σ criterion. 44 of the pixels have detected 1 cm emission in excess of 3σ, but most pixels are consistent with the estimated noise level.

Using equations (3) and (4), we can determine the expected free–free flux density in each of these pixels from both the 24 μm emission and L_{IR}. We plot histograms of the 1 cm emission with the estimated free–free contribution subtracted in Fig. 4(b), where it is clear that our estimate based on L_{IR} systematically overestimates the free–free emission while the estimate based on the 24 μm emission is generally consistent with the data. This is not unexpected as the total IR luminosity will also have a contribution from dust heated by an older stellar population not associated with free–free emission around H II regions. The pixels with excess emission after subtraction could have a significant AME contribution or particularly strong free–free or synchrotron emission. SED fitting is required to discriminate between these alternatives.

We estimate the spinning dust emission in each pixel using equation (11), and for illustration also estimate the emission using a spinning dust emissivity of 2×10^{-7} Jy/M_{PAH} implied by our fits to Enuc. 4. We present the histogram of AME-subtracted pixels for both emissivities in Fig. 4(c). It is clear that the ensemble of pixels are consistent with the spinning dust emission estimated by equation (11), but the Enuc. 4 emissivity severely overestimates the emission in most pixels even before subtracting a free–free component. In Fig. 4(d), we subtract both an estimate of the free–free based on $F_{\nu,24\,\mu\mathrm{m}}$ (equation 3) and an estimate of the spinning dust emission based on equation (11). Although agreement is overall good, the histogram is skewed negative, suggesting either the free–free, AME, or both have been overestimated. Additionally, outliers with residuals in excess of 3σ remain. This could imply either a strong AME component (similar to what is observed in Enuc. 4), regions in which our free–free estimate breaks down, or regions of particularly strong synchrotron emission.

To test whether the inclusion of an AME component is warranted by the data, we fit a model with only synchrotron and free–free emission to the SED of each pixel using the likelihood method described above. The 1 cm residuals from this fit are presented in Fig. 5(a), illustrating that the majority of pixels have a residual at 1 cm consistent with zero, i.e. an AME component is *not* needed to account for the 1 cm emission in these regions. We note, however, that the histogram of residuals is skewed negative, suggesting that the radio model is overestimating the 1 cm emission even before the inclusion of an AME component.

This tension can be alleviated somewhat if the synchrotron power law steepens between 3 and 1 cm. In Figs 5(c) and (d), we consider the most extreme case in which the synchrotron component drops to zero below 3 cm. That the fits continue to overestimate the 1 cm emission even in this case either suggests that the emission components are not being properly modelled at over wavelengths (particularly 3 and 6 cm) or that there is a calibration offset between the 1 cm data and some or all of the remaining points on the SED.

Given the uncertainty in the radio model, we cannot quantify precisely the AME in each pixel. However, as illustrated by Fig. 4(c),

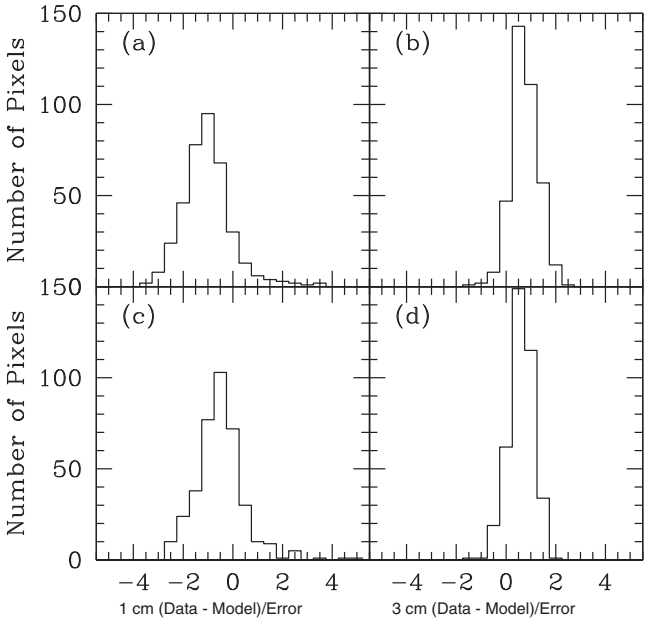

Figure 5. Fit residuals at 1 and 3 cm for radio models without an AME component. Panels (a) and (b) are for a constant synchrotron power-law index while panels (c) and (d) are for an index that steepens infinitely at 3 cm, resulting in no 1 cm synchrotron emission. Both models strongly indicate the need for an AME component in some regions. The asymmetry in the residuals for the former model suggest that the radio emission is being overestimated at 1 cm. This asymmetry is somewhat improved in the model with a steepening index, but some negative bias remains.

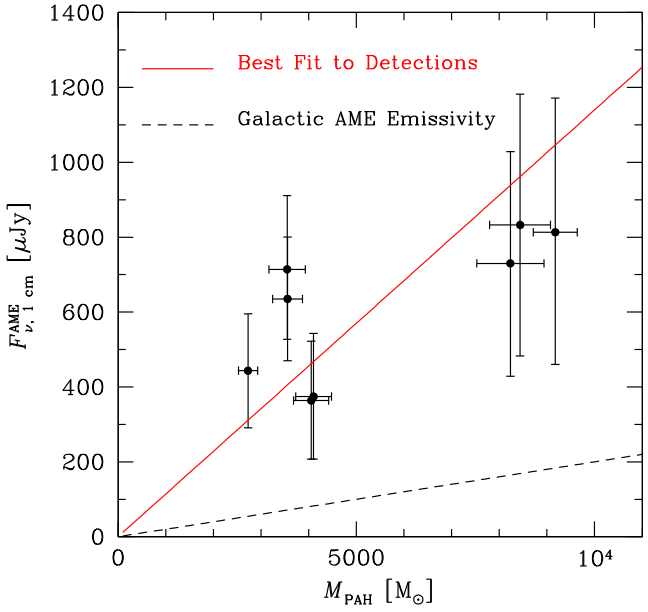

Figure 6. The PAH mass in each pixel in Table 2 is plotted against the fit AME flux density in that pixel. If the AME is arising from rotational emission from spinning grains, the two quantities should be roughly linearly correlated. We overplot the theoretical curve assuming linear correlation and using the canonical spinning dust emissivity (black dashed) as well as our best-fitting emissivity for the ensemble (red solid).

an emissivity per PAH mass consistent with that observed in Enuc. 4 is already ruled out from the 1 cm map alone. We can also constrain the AME in pixels with a subdominant radio component where the estimates of AME contribution are relatively insensitive to the synchrotron model, and we focus on these regions in the remainder of this section.

While the residuals plotted in Fig. 5 are helpful for identifying regions in which the free–free and synchrotron models are unable to produce enough emission at 1 cm to agree with observations, a residual fit will underestimate any true AME at 1 cm since other parts of the fit will be strained to accommodate a high 1 cm point. Thus, we perform two additional fits. First, we fit explicitly allowing a contribution from AME at 1 cm that may be either positive or negative. Secondly, we fit the data 3 cm and longwards with a radio model and estimate the AME as the fit residual at 1 cm. The agreement between these two methods is excellent.

Using a non-breaking synchrotron model, we identify three pixels having AME inconsistent with zero at 3σ and five additional pixels with AME significant at 2σ. If we allow no synchrotron contribution at 1 cm, we find two additional pixels significant at 2σ. The detections and their coordinates are listed in Table 2. We note that the pixels significant at 3σ are in the Enuc. 4 area. Three of the five pixels significant at 2σ are in the immediate vicinity of another star-forming region studied by Murphy et al. (2010, i.e. Enuc. 6). The remaining two are located in the extended region of relatively bright 1 cm emission to the north-east of Enuc. 4 (see Fig. 1).

4.2 AME per $M_{\rm PAH}$

Using equation (11) and the $q_{\rm PAH}$ and $M_{\rm d}$ values in each pixel as determined by Aniano et al. (2012), we predict the expected AME in each pixel from spinning dust emission. In Fig. 6, we plot the value of $M_{\rm PAH} = q_{\rm PAH} M_{\rm d}$ in each pixel against the 1 cm fit AME flux density $F^{\rm AME}_{\nu,1\,{\rm cm}}$ for the eight AME detections. The regions are

Table 2. AME detections.

Pixel	RA (J2000)	Dec. (J2000)	$F^{\rm AME}_{\nu,1\,{\rm cm}}$ (μJy)	$\frac{F^{\rm AME}_{\nu,1\,{\rm cm}}}{F_{\nu,1\,{\rm cm}}}$	$\frac{F_{\nu,100\,\mu{\rm m}}}{F^{\rm AME}_{\nu,1\,{\rm cm}}}$	$\frac{F_{\nu,8\,\mu{\rm m}}}{F_{\nu,24\,\mu{\rm m}}}$	$M_{\rm d}$ ($10^5\,M_\odot$)	$q_{\rm PAH}$	$L_{\rm d}$ ($10^7\,L_\odot$)	$\bar{U}$	$f_{\rm PDR}$	α	γ	$\alpha_{\rm sync}$
1	308.5885	60.1654	635 ± 170	0.62	1300	0.67	1.12	0.032	6.29	3.35	0.13	1.62	0.00	0.67
2	308.5768	60.1653	443 ± 150	0.61	1800	0.62	0.90	0.031	6.14	3.94	0.12	1.81	0.06	0.79
3	308.5885	60.1712	714 ± 200	0.55	1600	0.48	1.31	0.027	9.30	4.22	0.17	1.78	0.01	0.56
4	308.7644	60.1771	833 ± 350	0.56	2200	0.88	2.19	0.039	13.31	3.64	0.12	1.52	0.00	1.12
5	308.7527	60.1771	730 ± 300	0.57	2200	0.94	2.12	0.039	11.92	3.45	0.11	1.51	0.00	1.17
6	308.7644	60.1829	813 ± 360	0.49	3500	0.74	2.59	0.036	21.49	4.90	0.14	1.58	0.00	0.93
7	308.6119	60.1829	374 ± 170	0.46	1900	0.87	1.21	0.034	5.70	2.84	0.10	1.47	0.00	1.00
8	308.6236	60.1887	364 ± 160	0.63	1100	1.00	1.03	0.039	3.22	1.88	0.08	1.64	0.01	1.15

Note. RA and Dec. are reported at the centre of the 21 arcsec × 21 arcsec pixel. Thus, pixels in the same row or column of the gridded image will share an RA or Dec.

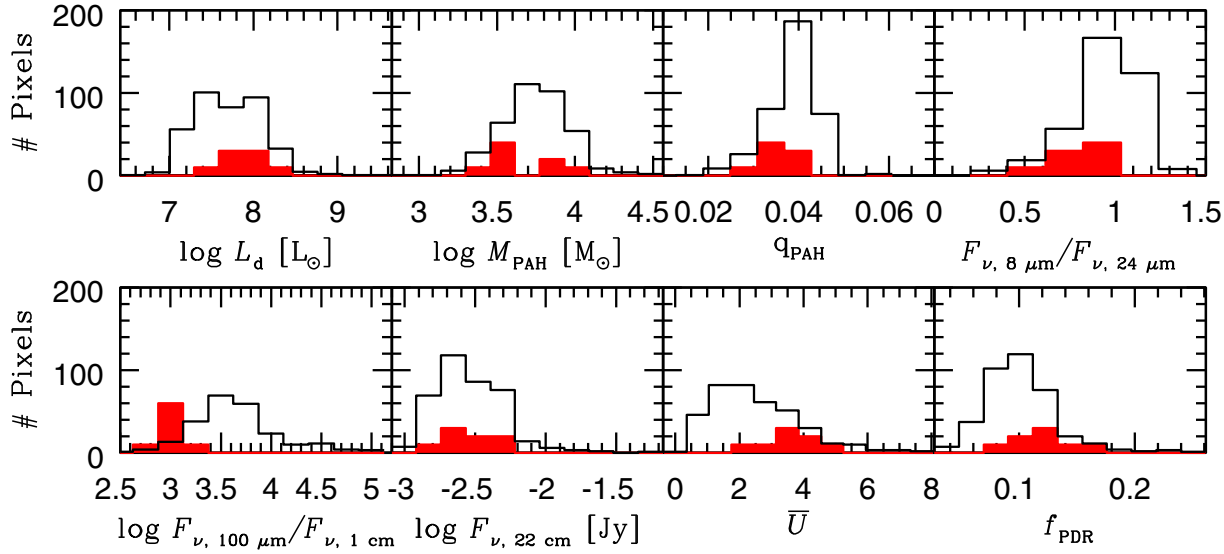

Figure 7. Histogram of various dust and environmental properties for the AME detections (red filled) and the ensemble of the pixels (black). For readability, we scale the number AME detections up by a factor of 10. Contrasting the two populations with a K-S test, the regions with AME detections favour larger $\bar{U}$ values with $p = 0.01$ and smaller $q_{\rm PAH}$ values with $p = 0.04$.

best fitted by an emissivity of $(1.1 \pm 0.2) \times 10^{-7}$ Jy/$M_{\rm PAH}$, in sharp tension with the 2×10^{-8} Jy/$M_{\rm PAH}$ typical of Galactic AME. Likewise, this value is too high to be consistent with the AME non-detections in the remainder of the galaxy as illustrated in Fig. 4(c). Therefore, if the AME is rotational emission from small spinning grains, the emissivity must vary significantly even at a fixed number of small grains.

4.3 AME detections versus non-detections

If some regions of the galaxy produce significantly more AME per PAH mass than others, what sets these regions apart? We contrast the AME detections against the ensemble of pixels in both dust properties ($L_{\rm d}$, $M_{\rm PAH}$, $q_{\rm PAH}$, $F_{\nu,8\,\mu{\rm m}}/F_{\nu,24\,\mu{\rm m}}$) and environmental properties ($F_{\nu,22{\rm cm}}$, $\bar{U}$, $f_{\rm PDR}$) in Fig. 7, where for clarity we have scaled up the number of AME detections in each bin by a factor of 10. Of particular note is that these regions appear to have *smaller* $q_{\rm PAH}$ and 8 to 24 μm ratio relative to the average value in the galaxy. A Kolmogorov–Smirnov (K-S) test indicates differences between the detections and the remainder of the pixels at >95 per cent confidence in both $q_{\rm PAH}(p = 0.04)$ and $\bar{U}(p = 0.01)$ whereas the remaining environmental parameters (aside from $F_{\nu,100\,\mu{\rm m}}/F_{\nu,1\,{\rm cm}}$) appear consistent between pixels with and without detections. However, we caution that the three detections in the Enuc. 4 area are not necessarily independent despite choosing pixels the size of the beam.

Performing a similar investigation within the Perseus molecular cloud, Tibbs et al. (2011) found that regions with AME tended to have stronger radiation fields than those without. Similarly, the strength of the radiation field was found to be correlated with the AME in the H II region RCW175 by Tibbs et al. (2012a). Observing AME in dark nebulae, AMI Consortium et al. (2009) also find that detections were correlated with the strength of the radiation field as inferred from the free–free emission. We also find a preference for larger $\bar{U}$ among our detections. Casassus et al. (2006) observed spinning dust emission in the photodissociation region (PDR) of LDN 1622, suggesting perhaps that spinning dust emission could be enhanced in these regions. We note that the physical scales in our study (≃1 kpc) are much larger than in these studies of Galactic clouds (≃1–10 pc). However, if the AME power is robust to environment as predicted by the spinning dust theory, we can make meaningful comparisons regardless of the size of the region. This is particularly true when comparing the AME power per $M_{\rm PAH}$.

The ratio of the AME flux density at 30 GHz to the 100 μm flux density has been a common diagnostic in the literature. Davies et al. (2006) at intermediate latitudes and Alves et al. (2010) in the Galactic plane both derive a value of 3×10^{-4}; Todorović et al. (2010) find a mean ratio of $(1.08 \pm 0.02) \times 10^{-4}$ in Galactic H II regions; and Planck Collaboration XV (2014b) derive values for Galactic clouds of $(2.5 \pm 0.2) \times 10^{-4}$ and $(5.8 \pm 0.7) \times 10^{-4}$ using an unweighted and weighted mean, respectively. An unweighted mean of the values in our Table 2 yields a ratio of $(5.1 \pm 1.8) \times 10^{-4}$, consistent with previous results though the variance is large. A large scatter in this quantity is unsurprising given the dependence of the 100 μm flux on grain temperature (Tibbs, Paladini & Dickinson 2012b).

We also note that the majority of pixels with a ratio of 100 μm to 1 cm flux density of less than ∼1000 are AME detections. While this in itself is unsurprising since regions with AME will be brighter at 1 cm than regions without, it suggests that this ratio could be a predictor of AME-positive regions using only these two bands.

There is also a distinct trend for the AME detections to be located in the spiral arms of the galaxy rather than the nuclear region. Additionally, it appears that there are large regions of AME emission that span multiple pixels, suggesting a 'diffuse' origin of the AME rather than, e.g. compact H II regions.

4.4 Correlations with AME intensity

We next examine correlations between the AME intensity and dust and environmental parameters. We find that, as expected, quantities that correlate with dust mass ($M_{\rm PAH}$, $L_{\rm d}$, $F_{\nu,100\,\mu{\rm m}}$) correlate with the fit AME intensity (Figs 6 and 8). Similarly, we find good correlations with the emission in all of the dust bands, in accord with observations of Galactic clouds by *Planck* (Planck Collaboration XV 2014b). Finally, we also observe positive correlation between

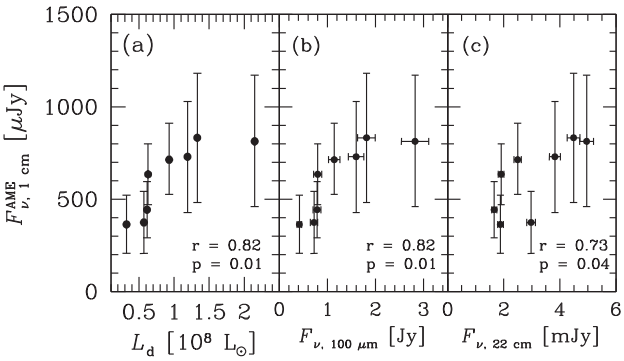

Figure 8. The fit AME flux density correlates positively with (a) the total dust luminosity L_d, (b) the 100 μm flux density (and the flux density in all IR bands), and (c) the 22 μm flux density (and the flux density in the other radio bands).

the AME intensity and emission in the radio bands, which is expected since both should correlate positively with the gas column. These correlations are summarized in Fig. 8.

To probe variations in AME strength beyond what is expected simply from the amount of gas and dust in that region, we normalize the fit AME flux density by the dust mass in that pixel. This is the normalization suggested by Tibbs et al. (2012b) who caution that the 100 μm flux, often used instead, is temperature-sensitive. This normalization is also directly comparable to the results of Planck Collaboration XV (2014b) where the optical depth at 250 μm τ_{250} was used as a normalization.

In Fig. 9, we plot M_d, q_{PAH}, $\bar{U}$, and f_{PDR} against the AME flux density normalized by the dust mass. Analysis of *WMAP* foregrounds by Lagache (2003) revealed that the AME per column decreases with increasing column, lending credence to the argument that AME is not arising from large grains. Planck Collaboration XV (2014b) reports a sublinear correlation between the AME intensity and the gas column with a power-law index of 0.33 ± 0.04. Likewise, studying AME in translucent clouds, Vidal et al. (2011) find that the AME intensity per gas column declines in proportion to the gas column. Among the AME detections in NGC 6946, we find a best-fitting power-law index of 0.59 ± 0.37, in accord with the results from Vidal et al. (2011) and Planck Collaboration XV (2014b), but limited by our small number of detections. The Pearson correlation coefficient likewise hints at a negative correlation between $F^{AME}_{\nu,1cm}/M_d$ and M_d.

Although we find tentative agreement with the previous result that the AME is imperfectly correlated with the large grains, we find no better correlation with tracers of small grains. The relationship between $F^{AME}_{\nu,1cm}/M_d$ and q_{PAH} is best fitted by a power-law index of -0.56 ± 0.62 whereas the value assumed by equation (11) is 1. The Pearson correlation coefficient also indicates a *negative* correlation between $F^{AME}_{\nu,1cm}/M_d$ and q_{PAH}. A similar result is obtained using the 8 to 24 μm ratio.

Ysard et al. (2010) find that over the whole sky the AME correlates better with the 12 μm emission than the 100 μm emission, although it was well correlated with both. Similarly Casassus et al. (2006) found the AME in the dark cloud LDN 1622 to be better correlated with maps of the 12–25 μm emission than the 100 μm emission. These trends are not observed in a study of Galactic clouds by Planck Collaboration XV (2014b), who find that the 12 μm map is less correlated with AME than maps at 25, 60, or 100 μm. As pointed out by Tibbs et al. (2012b), correlations against 100 μm are complicated by the dependence of the 100 μm flux on grain temperature. Likewise, the 12 μm emission depends not just upon the small grain population but also upon the strength of the radiation field. Taken together with our results, these data do not present a strong case for the association of AME with the smallest grains.

Previous work, both theoretical and observational, suggests an insensitivity of AME amplitude to the radiation field strength. In particular, Ysard & Verstraete (2010) find no correlation over three orders of magnitude in field strength. We likewise find no correlation, though our AME detections tend to be in regions of

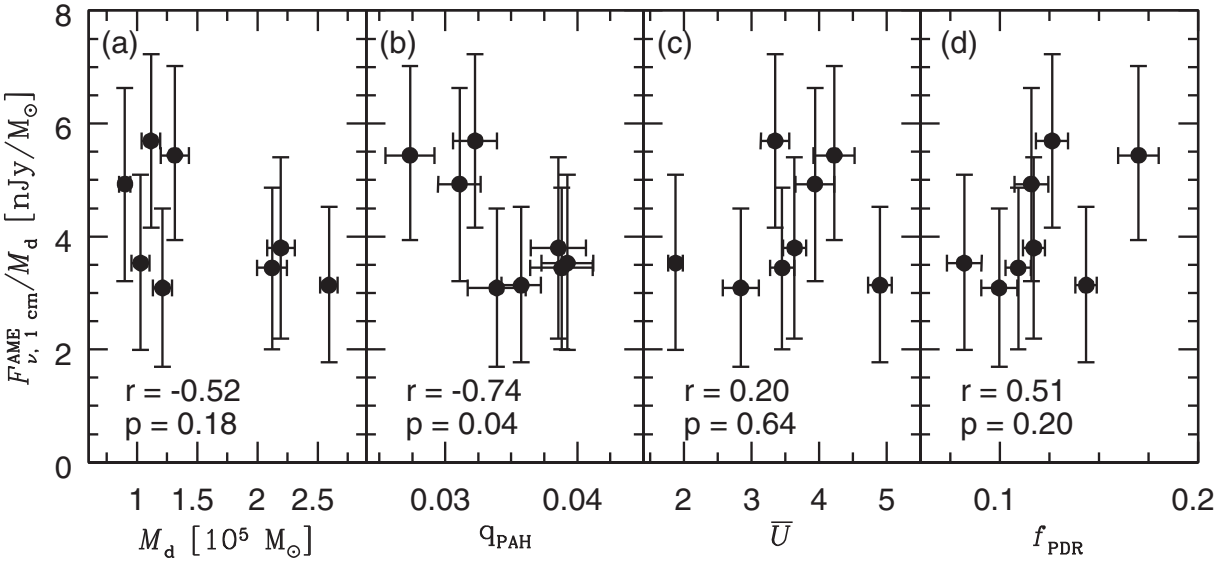

Figure 9. We examine the correlations between the environment and the strength of the AME per dust mass in the eight regions listed in Table 2. In all panels, we give the Pearson *r* coefficient and associated *p* value. As illustrated in panel (a), the AME flux density normalized by the dust mass is consistent with a negative correlation with dust mass, in accord with previous results that AME per column density decreases with column density. In panel (b), we find that a positive linear correlation with q_{PAH} is unfavoured by the data. We note that replacing q_{PAH} with the ratio of 8 to 24 μm emission produces a nearly identical plot. In the remaining panels, we find no correlations between the normalized AME flux density and (c) $\bar{U}$ or (d) f_{PDR}. However, the small sample size precludes drawing strong conclusions from the lack of any correlations.

above average radiation field intensity. We similarly find no significant correlation of the AME intensity with $f_{\rm PDR}$, though in both cases we are severely limited by the small number of detections.

5 DISCUSSION

The AME we observe in Enuc. 4 and several other regions of NGC 6946 is inconsistent with Galactic AME per dust mass even though the AME per 100 μm flux density in these regions falls within what has been observed in the Galaxy. Additionally, the emissivity per $M_{\rm PAH}$ in these regions is incompatible with upper limits on the AME in other regions of NGC 6946. Therefore, the data suggest strong variation of the AME intensity at fixed $M_{\rm PAH}$, a result unanticipated by theoretical models of spinning dust emission.

Although they did not estimate the population of small grains explicitly, Planck Collaboration XV (2014b) found a scatter of roughly an order of magnitude in the AME intensity normalized by the optical depth at 250 μm in a sample of Galactic clouds. Correlation analysis with a suite of environmental parameters yielded no compelling drivers of increased emissivity, much in accord with our results here.

Such variation is also evident in the Andromeda Galaxy, which has yielded only upper limits on an AME component despite observations with excellent frequency coverage from both *WMAP* and *Planck* and an ample dust reservoir in the galaxy (Ade et al. 2014). Recent determinations of the dust content of Andromeda by Draine et al. (2014) allow us to make a theoretical estimate of the expected spinning dust emission. Inserting the total derived dust mass of $5.4 \times 10^7\,{\rm M}_\odot$ and the global average value of $q_{\rm PAH} = 0.036$ from Draine et al. (2014), and a distance of 744 kpc (Vilardell et al. 2010) into equation (11) yields an AME flux density of 2.86 Jy. This value is comparable to the *total* observed 30 GHz emission of 2.55 ± 0.44 Jy and exceeds the 3σ upper limit placed on an AME contribution at that frequency of 2.2 Jy (Ade et al. 2014). However, the ratio of 100 μm to 30 GHz flux density is 7.1×10^{-4}, comparable to our detections and values obtained by Planck Collaboration XV (2014b).

Peel et al. (2011) investigate the SEDs of three dusty star-forming galaxies (M82, NGC 253, and NGC 4945) for evidence of AME. Using a benchmark AME to 100 μm flux density of 3×10^{-4}, they find AME flux densities estimated from this ratio far in excess of the observed emission for all three galaxies. This result would be exacerbated using instead the average value of 5×10^{-4} from our Table 2. Additionally, due to their excellent frequency coverage between 23 and 143 GHz, an AME component peaking at a frequency other than 30 GHz is unlikely to explain the missing flux.

In the context of spinning dust theory, the simplest explanation for variations in emission strength is variation in the abundance of small grains. However, this explanation is inconsistent with our data. We employ $q_{\rm PAH}$ directly from fits to the thermal dust emission to minimize spurious correlation induced by, e.g. varying grain temperatures. The AME is not found preferentially in regions with large values of $q_{\rm PAH}$, the 8 to 24 μm ratio, or even $M_{\rm PAH}$. Additionally, a linear scaling of the AME intensity per $M_{\rm d}$ with $q_{\rm PAH}$ is disfavoured by our data at greater than 2σ. If the spinning dust paradigm is correct, and if certain regions of NGC 6946 have AME much stronger than what has been observed in, e.g. Galactic clouds, then an explanation must be furnished for why the small grains in these regions are producing electric dipole radiation in excess of the expected level. Likewise, if the spinning dust emissivity in Andromeda is indeed much weaker than in the Milky Way despite comparable populations of small grains, this must too be explained.

We examine a few possibilities that may reconcile the variation in emissivity with the theoretical expectations, but none appear to be able to adequately resolve the tension. First, we have considered only the emission at 30 GHz, but AME has been observed over a range of peak frequencies from about 20 to 50 GHz (e.g. Planck Collaboration XV 2014b). It may be possible that regions like Enuc. 4 simply have AME peaking closer to 30 GHz than the typical diffuse ISM or Galactic clouds. However, if the AME were peaking at 20 GHz, the 30 GHz emission would be about two-thirds the peak value assuming the spectrum of equation (8). Likewise, if the AME peaked at 40 GHz, the 30 GHz amplitude would be lower than the peak amplitude by just over 10 per cent. This effect is insufficient to account for the entirety of the variation in Enuc. 4 and not permitted by the multifrequency observations of Andromeda (Ade et al. 2014) or the star-forming galaxies of Peel et al. (2011).

Second, the derived value of $q_{\rm PAH}$ does not correspond precisely to the total PAH fraction by mass. Rather, it is determined from the IR emission features and is therefore weighted towards regions with the high U value. Thus, if there were a reservoir of cold dust that was significantly depleted in PAHs (due, for instance, to grain coagulation), then the derived $q_{\rm PAH}$ would not reflect the true PAH mass of that region. However, the variations in $q_{\rm PAH}$ with environment required to reconcile the data with the theoretical emissivity would appear to be far greater than the observed pixel-to-pixel variations of $q_{\rm PAH}$ itself within the galaxy.

Third, $q_{\rm PAH}$ traces only the abundance of ultrasmall carbonaceous grains. If the AME arises in part or totally from ultrasmall grains of a different composition, such as ultrasmall silicates, then the abundance of AME-producing grains would not be accurately traced by $q_{\rm PAH}$. However, it is unclear why these grain populations would not vary cospatially nor does it seem likely that this could account for the entirety of the observed variations.

Finally, there exist mechanisms within the spinning dust theory that can alter the spinning dust emissivity. The typical electric dipole moment of a grain may vary from region to region due, for instance, to variations in grain asymmetry. However, we would expect these variations to be accompanied by environmental variations that explain the differences, such as a more intense radiation field, which we have not seen.

Taken in conjunction with the previous literature, our study suggests that the AME emissivity per $M_{\rm PAH}$ varies by more than a factor of 10 between the Andromeda Galaxy, the diffuse ISM of the Milky Way, Galactic clouds, and certain extranuclear regions of Enuc. 4. Without a clear means of discriminating between regions of particularly high or low AME, the spinning dust hypothesis is at best incomplete.

While we demonstrate the power of coupling AME observations with detailed modelling of the thermal dust component, we are limited by our frequency coverage and sensitivity. Follow-up observations that could better pin down the free–free component would be invaluable for more detailed SED modelling. In addition to mitigating a key uncertainty, such data would also allow exploration of the variations of the AME peak frequency with environmental parameters. Deeper 1 cm observations of NGC 6946 could better test whether the diffuse ISM of the galaxy has an AME emissivity consistent with equation (11).

6 CONCLUSIONS

We have combined new 1 cm and 3 mm CARMA observations and 2 mm GISMO observations with existing IR and radio data to

constrain the SED of the AME in NGC 6946. Our principal conclusions are as follows.

(i) We confirm the detection of AME by Murphy et al. (2010) in Enuc. 4 and find that the emission is well fitted by a spinning dust component having amplitude 0.9 mJy and peak frequency 42 GHz. The peak frequency corresponds well with models of the CNM and WIM. However, the emissivity exceeds the theoretical value by about a factor of 10 (3σ) given its PAH surface density.

(ii) We find eight regions with AME significant at >95 per cent confidence. Multifrequency follow-up observations of these regions are needed to confirm whether this excess is attributable to spinning dust emission. Such observations could further explore the spatial variations of the spinning dust emission within the galaxy, particularly dependence of the peak frequency on environment.

(iii) The strength of the AME in these regions is well correlated with all tracers of dust and gas mass, and we derive a spinning dust emissivity of 1×10^{-7} Jy/$M_{\rm PAH}$ in these regions, a factor of 5 higher than the Galactic value.

(iv) Our results are consistent with previous studies that suggest the AME per unit column density declines with increasing column density. We find no indication that AME positively correlates with the presence of small grains. We find that while regions with AME detections have preferentially more intense radiation fields, we find that the AME strength does not correlate with strength of the radiation field.

(v) The majority of locations in the galaxy are inconsistent with a spinning dust emissivity as strong as that observed in Enuc. 4 given their PAH surface density. This suggests that, if indeed the AME is emission from spinning ultrasmall grains, other environmental factors must influence the strength of the emission in ways not yet accounted for by spinning dust theory.

ACKNOWLEDGEMENTS

We thank John Carpenter for invaluable assistance reducing the CARMA data and Bruce Draine and the anonymous referee for extensive feedback that greatly improved the manuscript. We also thank Tim Brandt, Thiem Hoang, Chris Tibbs, and Chris White for helpful conversations.

BH acknowledges support from the NSF Graduate Research Fellowship under Grant no. DGE-0646086 and NSF grant AST-1408723. The GISMO observations and JS were supported through NSF ATI grants 1020981 and 1106284.

REFERENCES

Ade P. A. R. et al., 2014, preprint (arXiv:1407.5452)
Alves M. I. R., Davies R. D., Dickinson C., Davis R. J., Auld R. R., Calabretta M., Staveley-Smith L., 2010, MNRAS, 405, 1654
AMI Consortium et al., 2009, MNRAS, 400, 1394
Aniano G., Draine B. T., Gordon K. D., Sandstrom K., 2011, PASP, 123, 1218
Aniano G. et al., 2012, ApJ, 756, 138
Beck R., 2007, A&A, 470, 539
Bennett C. L. et al., 2003, ApJS, 148, 97
Braun R., Oosterloo T. A., Morganti R., Klein U., Beck R., 2007, A&A, 461, 455
Casassus S., Cabrera G. F., Förster F., Pearson T. J., Readhead A. C. S., Dickinson C., 2006, ApJ, 639, 951
Davies R. D., Dickinson C., Banday A. J., Jaffe T. R., Górski K. M., Davis R. J., 2006, MNRAS, 370, 1125
de Oliveira-Costa A., Kogut A., Devlin M. J., Netterfield C. B., Page L. A., Wollack E. J., 1997, ApJ, 482, L17
Dobler G., Draine B., Finkbeiner D. P., 2009, ApJ, 699, 1374
Draine B. T., Hensley B., 2012, ApJ, 757, 103
Draine B. T., Lazarian A., 1998a, ApJ, 494, L19
Draine B. T., Lazarian A., 1998b, ApJ, 508, 157
Draine B. T., Li A., 2007, ApJ, 657, 810
Draine B. T. et al., 2007, ApJ, 663, 866
Draine B. T. et al., 2014, ApJ, 780, 172
Hoang T., Draine B. T., Lazarian A., 2010, ApJ, 715, 1462
Hoang T., Lazarian A., Draine B. T., 2011, ApJ, 741, 87
Karachentsev I. D., Sharina M. E., Huchtmeier W. K., 2000, A&A, 362, 544
Kennicutt R. C., Jr et al., 2003, PASP, 115, 928
Kennicutt R. C. et al., 2011, PASP, 123, 1347
Kogut A., Banday A. J., Bennett C. L., Gorski K. M., Hinshaw G., Reach W. T., 1996, ApJ, 460, 1
Kovács A., 2008, in Duncan W. D., Holland W. S., Withington S., Zmuidzinas J., eds, Proc. SPIE Conf. Ser. Vol. 7020, Millimeter and Submillimeter Detectors and Instrumentation for Astronomy IV. SPIE, Bellingham, p. 70201S
Lagache G., 2003, A&A, 405, 813
Leitch E. M., Readhead A. C. S., Pearson T. J., Myers S. T., 1997, ApJ, 486, L23
Mathis J. S., Mezger P. G., Panagia N., 1983, A&A, 128, 212
Miville-Deschênes M.-A., Ysard N., Lavabre A., Ponthieu N., Macías-Pérez J. F., Aumont J., Bernard J. P., 2008, A&A, 490, 1093
Murphy E. J. et al., 2010, ApJ, 709, L108
Murphy E. J. et al., 2011, ApJ, 737, 67
Murphy E. J. et al., 2012, ApJ, 761, 97
Niklas S., Klein U., Wielebinski R., 1997, A&A, 322, 19
Peel M. W., Dickinson C., Davies R. D., Clements D. L., Beswick R. J., 2011, MNRAS, 416, L99
Planck Collaboration XVII, 2011a, A&A, 536, A17
Planck Collaboration XX, 2011b, A&A, 536, A20
Planck Collaboration 2014a, preprint (arXiv:1406.5093)
Planck Collaboration XV, 2014b, A&A, 565, A103
Planck Collaboration XVII, 2014c, A&A, 566, A55
Prieto J. L. et al., 2008, ApJ, 681, L9
Sault R. J., Teuben P. J., Wright M. C. H., 2011, Astrophysics Source Code Library, record ascl:1106.007
Scaife A. M. M. et al., 2010, MNRAS, 406, L45
Silsbee K., Ali-Haïmoud Y., Hirata C. M., 2011, MNRAS, 411, 2750
Staguhn J. et al., 2008, J. Low Temp. Phys., 151, 709
Staguhn J. G. et al., 2014, ApJ, 790, 77
Tibbs C. T. et al., 2010, MNRAS, 402, 1969
Tibbs C. T. et al., 2011, MNRAS, 418, 1889
Tibbs C. T. et al., 2012a, ApJ, 754, 94
Tibbs C. T., Paladini R., Dickinson C., 2012b, Adv. Astron., 2012, 124931
Todorović M. et al., 2010, MNRAS, 406, 1629
Vidal M. et al., 2011, MNRAS, 414, 2424
Vilardell F., Ribas I., Jordi C., Fitzpatrick E. L., Guinan E. F., 2010, A&A, 509, A70
Ysard N., Verstraete L., 2010, A&A, 509, A12
Ysard N., Miville-Deschênes M. A., Verstraete L., 2010, A&A, 509, L1

This paper has been typeset from a TEX/LATEX file prepared by the author.